

Isotropic 3D topological phases with broken time reversal symmetry

Hélène Spring^{1*}, Anton R. Akhmerov¹, Dániel Varjas^{2,3,4}

1 Kavli Institute of Nanoscience, Delft University of Technology, P.O. Box 4056, 2600 GA Delft, The Netherlands

2 Department of Physics, Stockholm University, AlbaNova University Center, 106 91 Stockholm, Sweden

3 Max Planck Institute for the Physics of Complex Systems, Nöthnitzer Strasse 38, 01187 Dresden, Germany

4 IFW Dresden and Würzburg-Dresden Cluster of Excellence ct.qmat, Helmholtzstr. 20, 01069 Dresden, Germany

*helene.spring@outlook.com

Abstract

Axial vectors, such as current or magnetization, are commonly used order parameters in time-reversal symmetry breaking systems. These vectors also break isotropy in three dimensional systems, lowering the spatial symmetry. We demonstrate that it is possible to construct a fully isotropic and inversion-symmetric three-dimensional medium where time-reversal symmetry is systematically broken. We devise a cubic crystal with scalar time-reversal symmetry breaking, implemented by hopping through chiral magnetic clusters along the crystal bonds. The presence of only the spatial symmetries of the crystal—finite rotation and inversion symmetry—is sufficient to protect a topological phase. The realization of this phase in amorphous systems with average continuous rotation symmetry yields a statistical topological insulator phase. We demonstrate the topological nature of our model by constructing a bulk integer topological invariant, which guarantees gapless surface spectrum on any surface with several overlapping Dirac nodes, analogous to crystalline mirror Chern insulators. We also show the expected transport properties of a three-dimensional statistical topological insulator, which remains critical on the surface for odd values of the invariant.

1 Introduction

A three-dimensional (3D) isotropic medium has the highest degree of spatial symmetry. Unless they are explicitly broken, non-spatial symmetries like time-reversal symmetry (TRS) are also present in isotropic systems. Removing TRS typically also breaks isotropy, for example ferromagnets break TRS but also break rotation symmetry along the axes which are not parallel to the magnetization. Antiferromagnets restore some spatial symmetries such as the product of inversion and TRS, but also break rotation symmetry [1]. The spatial symmetries are partially restored in altermagnets [2]—a recently proposed class of materials combining lack of net magnetization with a spin splitting away from away from high-symmetry momenta, however even in these materials the magnetic order

is incompatible with full isotropy.

The spatial symmetries of a system are relevant both for defining and protecting topological phases [3–6]. While initially considered to be susceptible to disorder, topological systems relying on spatial symmetries were later shown to be protected from localization as long as the disordered ensemble respects the spatial symmetries [7–9]. This protection by an ‘average’ symmetry, a hallmark of statistical topological insulators, is especially powerful in isotropic amorphous media. In an earlier work we demonstrated that unlike their crystalline counterparts—where the spatial symmetry is only preserved by certain crystal terminations—it is possible to utilize the isotropy of a 2D amorphous medium to extend the topological protection to any edge of the system [10].

Motivated by the two above considerations, we ask whether it is possible to find a model hosting a topological phase protected only by spatial symmetries. Because both TRS and average TRS protect topological phases, we additionally require that the desired model also breaks TRS on average. By designing a scalar, rather than a vector TRS breaking order, we answer positively to the above question. Specifically we demonstrate that the spatial symmetries present in 3D isotropic media protect topological phases, and that the amorphous realization of such a system is a statistical topological insulator phase.

The organization of the manuscript is as follows. In Sec. 2 we formulate an isotropic continuum model where TRS is systematically broken. We present a microscopic Hamiltonian that replicates this model when assembled into a crystal structure, and we present results for the amorphous realization of this model. In Sec. 3 we demonstrate the topological nature of our models by formulating bulk invariants, examining surface dispersions, and analyzing transport of the topologically protected surface modes. As established in the study of statistical topological insulator phases, we show that the model localizes when its degrees of freedom are doubled. We conclude in Sec. 4.

2 Symmetry analysis

2.1 Continuum model

In order to guide the construction of a microscopic model, we begin from developing a minimal continuum model with the desired symmetries using the software package Qsymm [11]. We follow the procedure outlined in Ref. [10]. We start by generating a minimal 2D Dirac Hamiltonian. The mass terms present in this minimal Hamiltonian are capable of gapping out the spectrum. We then search for all of the symmetry representations of inversion and continuous rotation symmetry that remove the mass terms of the minimal Hamiltonian, thereby ensuring that the spatial symmetries prevent a gap from opening. These 2D Hamiltonians correspond to the surfaces of 3D topological bulk models in the same symmetry class. By utilizing the isotropy, we extend the symmetry representations from 2D to 3D to obtain the 3D bulk phases. The symmetry representations of the spatial symmetries are listed in App. A, Eq. (A.1) and (A.2). The resulting k -space model is of the form:

$$H_{4\times 4}(\mathbf{k}) = (\mu_1 + t_2 k^2)\sigma_0(\tau_0 + \tau_z)/2 + (\mu_2 + t_3 k^2)\sigma_0(\tau_0 - \tau_z)/2 + (-t_1 + t_4 k^2)\boldsymbol{\sigma} \cdot \mathbf{k}\tau_y + (-t_0 + t_5 k^2)\boldsymbol{\sigma} \cdot \mathbf{k}\tau_x, \quad (1)$$

where μ_i are chemical potential terms, t_i are the hopping terms, σ and τ are the Pauli matrices, with τ representing the orbital space and σ representing spin space, $\mathbf{k} = (k_x, k_y, k_z)$, and $k^2 = \mathbf{k} \cdot \mathbf{k}$.

Limiting the model to terms quadratic in k means a k -dependent transformation of the form $\exp(i\sigma_z\phi)$ is capable of removing the relative hopping phases and restoring a

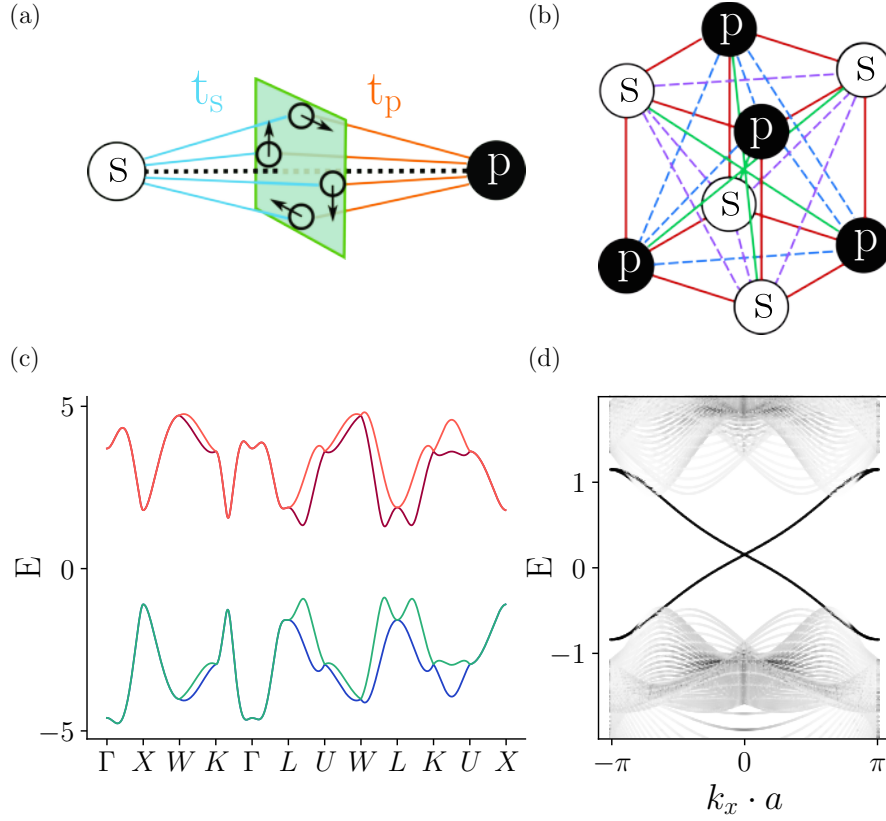


Figure 1: Time-reversal symmetry breaking in a microscopic system with inversion and rotation symmetry. (a) A bond between s and p orbitals hosting four mid-bond s orbitals (on plane shown in green) that host magnetic moments. (b) A section of a rock salt crystal structure made from the bond shown in (a). Red lines indicate nearest-neighbor hopping between s and p orbitals, dashed lines indicate next-nearest neighbor hopping between s (purple) and p (blue) orbitals, green lines indicate next-next-nearest neighbor hopping between s and p orbitals. (c) The bulk dispersion relation obtained from the crystal structure shown in (b) along the high-symmetry points of the face-centered cubic Brillouin zone. Different colors indicate different bands. (d) Bulk and surface dispersion of a 3D slab of the crystal. Darker color indicates a larger participation ratio. Plot details are in App. B.

TRS-like symmetry. Therefore, the model includes terms up to k^3 in order to remove this residual symmetry.

Despite lacking TRS, the high degree of spatial symmetry of this model protects the twofold spin degeneracy of all bands. For a fixed \mathbf{k} , the eigenstates of (1) are eigenstates of the angular momentum operator in the direction parallel to \mathbf{k} . Mirror symmetry exchanges states with opposite angular momentum, thereby ensuring the degeneracy of the spin bands.

2.2 Microscopic implementation

Based on the symmetry-allowed terms of the continuum model (1), we now construct a microscopic model that preserves isotropy while breaking TRS. The minimal model contains two orbitals that have opposite inversion eigenvalues, which we choose as an s and a p orbital. We choose the σ degree of freedom to correspond to the electron spin,

which makes the last four terms of Eq. (1) spin-orbit-like, although with an additional k -dependent phase shift necessary to break TRS. In order to realize these spin-orbit-like hoppings in a microscopic model, we therefore consider two separate atoms that host spinful s and $p_{x,y,z}$ orbitals respectively, as illustrated in Fig. 1(a). For the purpose of obtaining a minimal model, we separate the p orbitals into $p_{3/2}$ and $p_{1/2}$ orbitals with an atomic spin-orbit coupling, and consider only the lower-energy $p_{1/2,\uparrow\downarrow}$ subspace.

In order to break TRS, we introduce magnetic atoms between the s and p orbitals. Hopping between the two atoms occurs through a virtual process via four s orbitals on a plane perpendicular to the s - p bond axis, located on the middle of the bond [Fig. 1(a)]. These intermediate s orbitals each host a magnetic moment, such that together they form a chiral magnetic texture in the plane that contains them. The curl of the magnetic texture defines a TRS-odd vector, that combined with the hopping vector \mathbf{r} , defines a scalar quantity $(\nabla \times \mathbf{M}) \cdot \mathbf{r}$. This is the desired source of scalar TRS breaking. Tiling the space with such s - p bonds restores spatial symmetries, while keeping TRS broken.

The Hamiltonian of an x -aligned s - p bond is:

$$H_m = E_s \sum_{\sigma} |s_{\sigma}\rangle \langle s_{\sigma}| + E_p \sum_{i,\sigma} |p_{i\sigma}\rangle \langle p_{i\sigma}| + \sum_{n,\sigma} (\Delta |s_{n\sigma}\rangle \langle s_{n\sigma}| + t_s |s_{\sigma}\rangle \langle s_{n\sigma}| + \text{h.c.}) \\ + \sum_{i,n,\sigma} (t_{in} |p_{i\sigma}\rangle \langle s_{n\sigma}| + \text{h.c.}) + \alpha \hat{\mathbf{L}}_p \cdot \hat{\boldsymbol{\sigma}}_p + \sum_n \mathbf{B}_n \cdot \hat{\boldsymbol{\sigma}}_n, \quad (2)$$

where $\sigma \in \{\uparrow, \downarrow\}$, $i \in \{x, y, z\}$, $n \in \{1, 2, 3, 4\}$, $|s_{\sigma}\rangle$ are the spinful s orbital states, $|s_{n\sigma}\rangle$ are the mid-bond magnetic s_n orbitals, $|p_{i\sigma}\rangle$ are the $p_{x,y,z}$ orbitals, $E_{s/p}$ are the onsite energies of the s and p orbitals, Δ is the onsite energy of the mid-bond s_n orbitals, α is the magnitude of the atomic spin-orbit coupling splitting on the p orbitals, $\hat{\boldsymbol{\sigma}}_{p/n}$ are the spin operators on the p and s_n orbitals, $\hat{\mathbf{L}}_p$ are the orbital angular momentum operators on the p -orbitals, \mathbf{B}_n are the magnetic moments of the s_n orbitals. Finally, t_{in} are the amplitudes of the s_n - p_i hopping, determined by whether the hopping between the $p_{x,y,z}$ orbitals and the s_n orbitals takes place via the positive or negative lobes of the p orbitals:

$$t_{in} = t_x \delta_{ix} + t_{yz} \delta_{iy} \text{sgn}(y_n) + t_{yz} \delta_{iz} \text{sgn}(z_n) \quad (3)$$

where y_n and z_n are the y and z coordinates of the s_n orbitals and $\text{sgn}(0) = 0$.

We use the Python software package Pymablock [12] to obtain the effective hopping t_{sp} between the s and $p_{1/2}$ orbitals as a second-order perturbation. We find that the resulting terms have the desired symmetries by substituting in arbitrary parameters. We demonstrate this result in a limiting case defined by the set of inequalities $\alpha \gg \Delta + B \gg \Delta - B \gg E_s, E_p - \alpha, t_s, t_{x/y/z}$, which holds when spin-orbit coupling is large, and hopping only occurs via the lower-energy virtual level $\Delta - B$. The resulting expression for the effective hopping amplitude is:

$$t_{sp} = \frac{t_s(2t_x - it_{yz})}{\sqrt{3}(\Delta - B)} i\sigma_x. \quad (4)$$

This hopping has a complex hopping phase, which breaks TRS. In order to ensure that the hopping phase cannot be removed by a global basis-transformation introducing a relative phase between the s and p wavefunctions, the hopping phase must be distance dependent. This arises naturally due to the different distance dependence of the microscopic hopping amplitudes from the p_x and $p_{y,z}$ orbitals. Hopping terms along directions other than x follow from applying rotation operators, resulting in hopping terms proportional to $\mathbf{d} \cdot \boldsymbol{\sigma}$ where \mathbf{d} is the hopping vector.

2.3 Spin splitting in a crystal

Because the scalar TRS breaking is insufficient to cause a spin splitting in an isotropic medium, we demonstrate the spin splitting in a crystal structure. We use the s and p atoms as the basis of the rock salt crystal structure [Fig. 1(b)] with full cubic (O_h) symmetry. In this model, orbitals of the same type are connected by normal hopping, and orbitals of different types are connected by the complex spin-orbit hopping of (4), resulting in terms off-diagonal in the orbital (τ) space. Because the symmetry-breaking mechanism relies on the nontrivial distance-dependence of the hopping phase, we include both nearest-neighbor as well as third-nearest-neighbor s - p hopping [Fig. 1(b)]. The tight-binding Hamiltonian thus takes the form:

$$\begin{aligned}
 H_{\text{salt}} = & \left(\mu_1 + t_1 \sum_{\mathbf{d}_2} e^{i\mathbf{k}\cdot\mathbf{d}_2} \right) \sigma_0(\tau_0 + \tau_z)/2 + \left(\mu_2 + t_2 \sum_{\mathbf{d}_2} e^{i\mathbf{k}\cdot\mathbf{d}_2} \right) \sigma_0(\tau_0 - \tau_z)/2 \\
 & + \frac{i}{a} \left(\sum_{\mathbf{d}_1} e^{i\mathbf{k}\cdot\mathbf{d}_1} \mathbf{d}_1 \cdot \boldsymbol{\sigma} \right) (t_3\tau_+ + t_3^*\tau_-) + \frac{i}{a} \left(\sum_{\mathbf{d}_3} e^{i\mathbf{k}\cdot\mathbf{d}_3} \mathbf{d}_3 \cdot \boldsymbol{\sigma} \right) (t_4\tau_+ + t_4^*\tau_-),
 \end{aligned} \tag{5}$$

where a is the cubic cell lattice constant, $\sigma_{\pm} = \frac{1}{2}(\sigma_x \pm i\sigma_y)$, and similarly for τ_{\pm} . \mathbf{d}_1 runs over the six nearest-neighbor bonds symmetry-equivalent to $\frac{a}{2}(1, 0, 0)$, \mathbf{d}_2 over the twelve next-nearest neighbor bonds symmetry-equivalent to $\frac{a}{2}(1, 1, 0)$, and \mathbf{d}_3 over the eight next-next-nearest neighbor bonds symmetry-equivalent to $\frac{a}{2}(1, 1, 1)$. The terms of Eq. (5) proportional to t_1 and t_2 are the next-nearest neighbor s - s and p - p normal hoppings respectively [dashed lines of Fig. 1(b)], where t_1 and t_2 are both real. The terms proportional to t_3 and t_4 are the nearest and next-next-nearest neighbor s - p hoppings respectively [solid lines of Fig. 1(b)], with t_3 and t_4 complex. This Bloch Hamiltonian reproduces the symmetry-allowed terms of the continuum model (1) in the long-wavelength limit, aside from an additional cubic anisotropy term and a slight change of parametrization.

The tight-binding model (5) preserves the space group of the rock salt crystal structure [see App. A]. The spin-orbit-like s - p hopping terms alternate in sign along the hopping axes in order to preserve inversion symmetry. We select the parameters $\mu_1 = 0.1$, $\mu_2 = 0.2$, $t_1 = 0.3$, $t_2 = -0.4$, $t_3 = \exp(0.3i)$, $t_4 = 0.2i \exp(0.3i)$. The dispersion relation shows that the spin bands are split away from high-symmetry points and lines that have at least a rotation and a mirror symmetry, demonstrating that TRS is broken [Fig. 1(c)]. The TRS-breaking terms of our model are next-next-nearest neighbor terms, which leads to linear TRS-breaking terms intrinsically cancelling out and only cubic terms remaining. The surface dispersion shows gapless, propagating surface modes within the bulk gap [Fig. 1(d)].

2.4 Amorphous realization

Amorphous systems possess average continuous rotation symmetry, average reflection and average inversion [10]. Since the scalar TRS-breaking mechanism is independent of bond orientation, an amorphous realization of the crystal model (5) possesses ensemble isotropy while also systematically breaking time-reversal.

We construct amorphous systems using the same procedure as in Ref. [10], treating system sites as hard spheres. Rather than simulating an amorphous version of the crystal defined in Sec. 2.3, with two families of atoms and two degrees of freedom per atom, for simplicity and without loss of generality we simulate one type of atom with four degrees of freedom. We define a minimal real-space model using Qsymm. To further examine the

extent of topological protection, we also define a model with twice the degrees of freedom and two protected Dirac cones on the surface in the continuum limit (see App. A for the full definition of both models). We examine the spectral functions of the minimal model, and confirm the joint presence of a spectral gap and the lack of spin splitting [Fig. 2(a)], as expected from the symmetry analysis of the continuum model. The surface spectral function confirms the presence of gapless surface modes within the bulk gap [Fig. 2(b)].

3 Topological properties

3.1 Bulk invariants

To define the topological invariants, we observe that the high spatial symmetry guarantees that the protected band gap closings only occur at high symmetry momenta: $\mathbf{k} = \mathbf{0}$ and $\mathbf{k} = \infty$ for the amorphous system. To compute the k -space topological invariant we use an effective k -space Hamiltonian H_{eff} that we obtain by inverting the single-particle Green's function that we project onto the plane wave basis, as described in Refs. [6, 10, 13].

The invariants of 3D statistical topological insulators are constructed from the invariants of 2D strong topological phases [9]. The invariant of 2D class A systems is the Chern number, given by the integral of the Berry curvature over the 2D Brillouin zone at the Fermi energy. Our 3D class A model relies on mirror symmetry to protect its surface modes. Therefore a possible bulk invariant of this model is a mirror Chern number, given by the difference in Chern numbers of opposite mirror sectors:

$$C_M = \frac{1}{2}(C_+ - C_-), \quad C_{\pm} = \iint \mathcal{F}_{\pm}(\mathbf{k}) d^2\mathbf{k}, \quad (6)$$

where the integral runs over a compactified mirror-invariant plane $\mathbb{R}^2 \cup \{\infty\}$ [10, 13] (e.g. $k_z = 0$, invariant under the mirror operator $k_z \rightarrow -k_z$ with $U_{M_z} = \mathcal{I} \exp(i\pi S_z)$), and \mathcal{F}_{\pm} is the Berry curvature of the even/odd ($\pm i$ eigenvalue) mirror sub-blocks of the Hamiltonian. The invariant for crystal systems has the same form for a mirror-invariant plane in the crystal Brillouin zone [3]. However, because both the systems have inversion and rotation symmetries, the mirror Chern number can also be expressed in terms of rotation and inversion eigenvalues at high-symmetry momenta. Numerical results and a further discussion of invariants of the amorphous system are found in App. C.

3.2 Surface spectrum

As demonstrated in Fig. 1(d) for the crystalline system, the high-symmetry surface of the $C_M = 1$ model hosts a single Dirac cone, and multiple Dirac cones remain protected for $C_M > 1$. We expect that the high degree of ensemble averaged spatial symmetry of the amorphous Hamiltonian prevents surface states from being gapped out on any surface both for the single and doubled model ($C_M = 1$ and 2 respectively). We confirm this by numerically computing the surface spectral function

$$A(E, \mathbf{k}) = \sum_l \langle \mathbf{k}, l | \delta(H - E) | \mathbf{k}, l \rangle, \quad (7)$$

using the Kernel polynomial method [10, 14, 15]. Here H is the real-space Hamiltonian of a finite slab, l runs over the internal degrees of freedom, and $|\mathbf{k}, l\rangle$ is a plane-wave state localized on one surface.

Both the original and doubled amorphous models have a nonzero surface density of states in the bulk gap, with one or two Dirac nodes located at zero momentum.

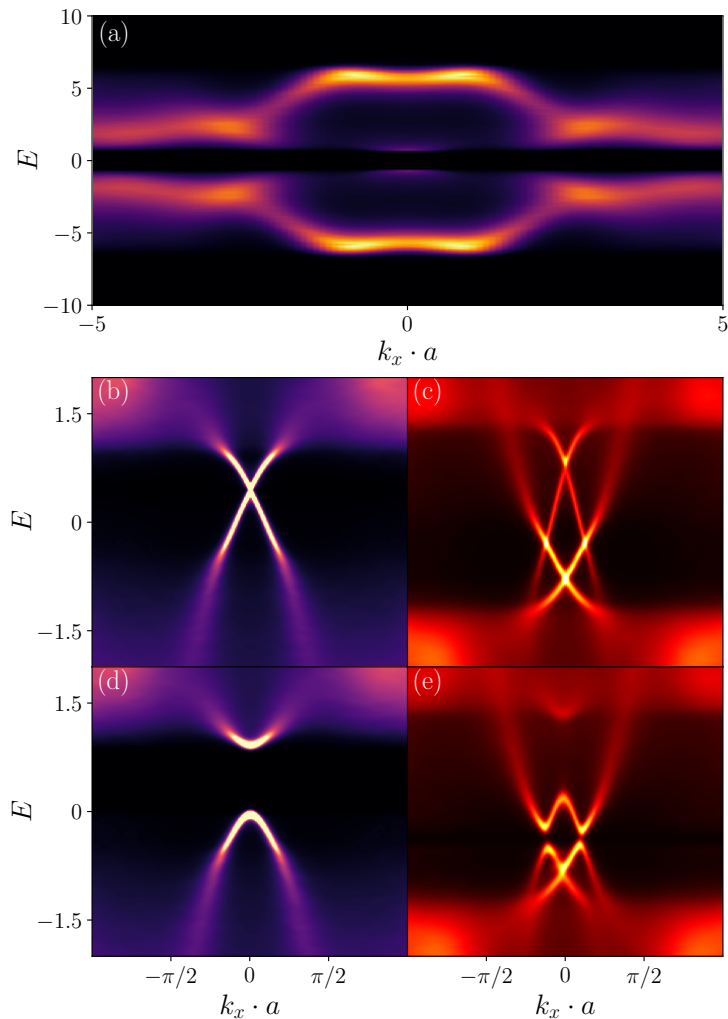


Figure 2: The (a) bulk and (b)-(e) surface spectral functions of the amorphous models. (b)-(c) The surface spectral functions of the single Dirac cone model (A.4) and the double Dirac cone model (A.8). (d)-(e) the same models as (b)-(c) but with broken spatial (mirror and rotation) symmetries. Plot details are in App. B.

[Fig. 2(b,c)]. This is a consequence of the nontrivial topology of the effective Hamiltonian, or equivalently, of the disorder-averaged Green's function. The surface spectral function in the k_x direction probes the topology of the $k_y = 0$ cut of the bulk effective Hamiltonian, which is invariant under M_y in the thermodynamic limit. This allows decomposition into two mirror sectors, each of which is a Chern insulator, resulting in an edge spectrum with C_M pairs of counter-propagating chiral edge states crossing the bulk gap. The modes with different chirality correspond to different mirror sectors, hence they are protected from gapping out by disorder that respects the mirror symmetry on average. The surface states are insensitive to the details of the boundary, and only gap out when the symmetries protecting the topological phase (rotations and mirrors normal to the surface) are broken on average [Fig. 2(d,e)].

3.3 Surface transport

Reference [9] conjectures that only the \mathbb{Z}_2 part of the invariant provides topological protection, or in other words, that only the surface states of systems with odd C_M are pro-

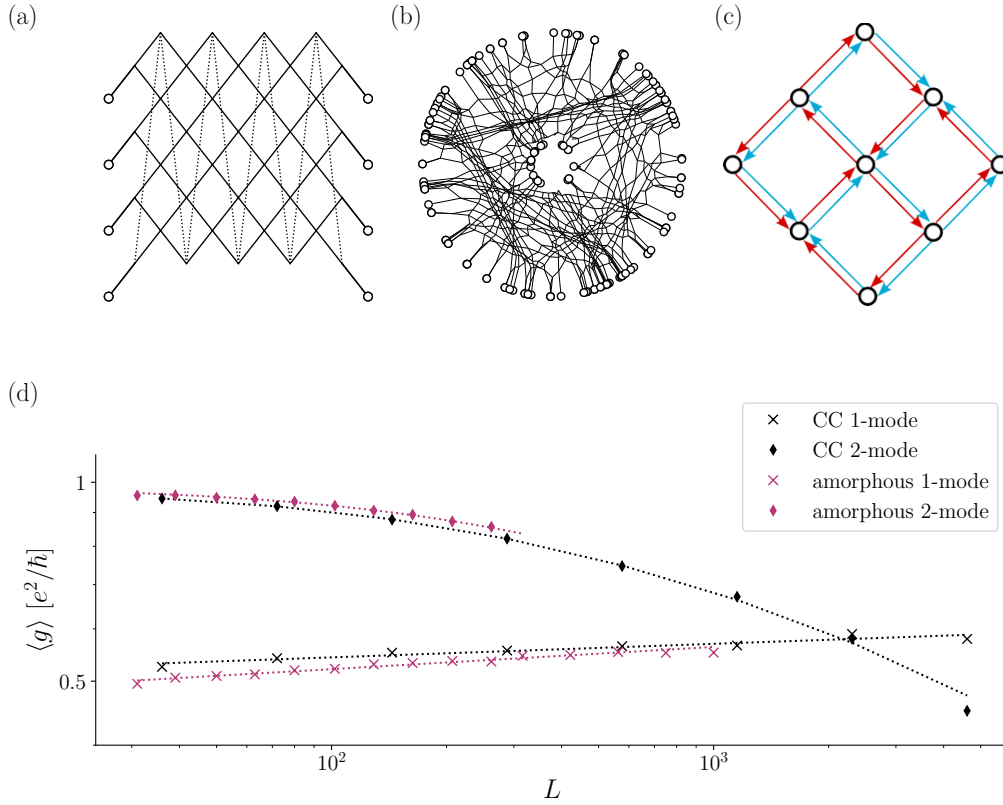


Figure 3: Conductivity of translationally invariant and amorphous networks. (a) Schematic of the Chalker-Coddington model. Dashed links loop in the vertical direction to indicate periodic boundary conditions. Circular nodes indicate external nodes where modes enter and exit the network. Internal nodes are located at all solid line crossings. (b) Schematic of the amorphous network. Circular nodes indicate external nodes where modes enter and exit the network. Nodes internal to the network are located at all line crossings. (c) Schematic of modes in the doubled model. (d) Average conductivity of the networks as a function of network length and width L and fits (dashed lines). Results are shown for the Chalker-Coddington (CC) network and amorphous network, with 1 mode per link (crosses) and 2 modes per link (diamonds). Plot details are in App. B.

tected from localization. In a crystalline system, the surface has an ensemble point group symmetry, and its localization properties are therefore equivalent to a doubled Chalker-Coddington network model, which has a localized phase with an anomalously large localization length [16, 17]. The conjecture, however, was not confirmed for 3D phases with continuous rotation symmetries, such as our amorphous model. To confirm the conjecture, we simulate the surface transport properties using amorphous network models.

We first simulate the transport properties of the regular network model as a baseline for the comparison. In the presence of disorder that preserves the spatial symmetries on average, the surface of the crystalline phase is equivalent to a critical Chern insulator. We simulate its transport properties with the Chalker-Coddington network model on the square lattice [18]. We fix the aspect ratio of the network to 1 and impose periodic boundary conditions along the y direction [Fig. 3(a)]. The scattering matrices at each node of the network are random 2×2 matrices sampled from a Haar-distributed $U(2)$

ensemble. The conductance through the system is:

$$G = \frac{e^2}{h} \sum_i T_i, \quad (8)$$

where T_i are the transmission probabilities from the modes entering one side of the network to the modes exiting on the other side. Since the aspect ratio equals to 1, the system conductivity $g = G$. We calculate the average conductivity $\langle g \rangle$ as a function of system size L and reproduce the known result $\langle g \rangle \approx 0.5\text{--}0.6e^2/\hbar$ [19] [Fig. 3(d)], with the slow increase as a function of L due to finite-size effects. We investigate the localization properties of the double Dirac cone model by doubling the number of modes on each link, as shown schematically in Fig. 3(c). This system is expected to localize, based on both numerical [16] and analytical [17] studies. We draw the 4×4 scattering matrices of the doubled networks from the circular unitary ensemble and confirm localization at system sizes of several thousand sites [Fig. 3(d)].

We now simulate the conductance of our amorphous model, in order to determine whether the average continuous rotation symmetry has an effect on the conductance properties of the system. We define an amorphous 2D network model in order to simulate the average rotation symmetry using a fourfold coordinated random graph [13, 20], for details of the construction of the amorphous network see App. D. We use an annulus geometry in order to avoid issues constructing the network with periodic boundary conditions, and numerically calculate the conductance through the bulk from the modes entering the outer edge to the modes exiting the inner edge of the annulus [Fig. 3(b)]. The conductance G is calculated using (8), and the conductivity of the annulus equals:

$$g = \frac{1}{2\pi} G \log \left(\frac{R}{r} \right), \quad (9)$$

where R and r are the outer and inner radii of the annulus respectively. The results for the amorphous network closely follow the results for the regular network: the single Dirac cone conductivity falls within the $0.5 - 0.6e^2/\hbar$ range for small L and increases due to finite-size effects, and the double Dirac cone network localizes [Fig. 3(d)]. These observations confirm that a doubled phase transition is not protected from localization, even in the presence of average isotropy.

4 Conclusion and discussion

In this work, we found that 3D isotropic systems breaking all non-spatial symmetries host topologically protected phases of matter. We devised a rotation- and inversion-symmetric continuum model with broken time-reversal symmetry, and presented a microscopic realization of this model in amorphous matter with average isotropy. We constructed a bulk \mathbb{Z} invariant—expressible both in terms of symmetry eigenvalues and mirror Chern numbers—corresponding to the number of protected ungapable surface Dirac cones, which we numerically demonstrated.

We simulated the transport of our models using both regular and amorphous network models with random scattering at each node. We found results consistent with critical scaling, deviations from which are likely due to finite-size effects. Upon doubling the degrees of freedom in both the regular and amorphous networks, the modes localize as conjectured in Refs. [9, 16, 17]. Even though any number of surface Dirac cones are protected from gapping out, only an odd number are protected from localization.

Due to the combination of average continuous rotation symmetry and inversion symmetry, the spin bands in the bulk of the amorphous system are doubly degenerate. This

raises the question whether the systematic breaking of TRS leads to a macroscopic change in the material properties. Enumerating the possible non-dissipative electromagnetic responses compatible with isotropy and inversion-symmetry, but forbidden by TRS, we find $\mathbf{P} \propto \mathbf{E} \times \mathbf{B}$, electrical polarization parallel to the Poynting vector. This second-order response is distinct from the circular photogalvanic effect [21, 22], which only manifests in systems with broken inversion symmetry, and should therefore be absent in our system. The combination of these two responses therefore serve as a probe of the scalar TRS breaking.

A natural further question is, what is the classification of isotropic three-dimensional media with or without inversion symmetry in the other Altland-Zirnbauer symmetry classes [23]. The topological invariants outlined in this work remain valid if we also include TRS besides isotropy and inversion symmetry. Our models are compatible with prescribing TRS with the usual representation $\mathcal{T} = \exp(i\pi S_y)\mathcal{K}$, which fixes some parameters, but does not forbid any topological phases. In this case odd values of C_M correspond to an amorphous strong topological insulator [24], however, the gapless surface Dirac cones remain protected by mirror symmetry for even values as well. To our knowledge, TRS does not enrich the classification in the presence of isotropy and inversion symmetry; and the classification with isotropy, broken inversion and unbroken TRS is the same as the strong \mathbb{Z}_2 classification with TRS only. There is, however an interesting possibility that isotropy and the protection of the surface density of states in a doubled phase prevents the surface conductivity from going below the metal-insulator critical point, and because of that guaranteeing that the surface stays metallic. We leave an investigation of these properties to future work.

Our microscopic model—relying on orbital-selective hoppings through chiral magnetic molecules—demonstrates the difficulty of constructing a time-reversal odd, inversion even, scalar order parameter. In our case the order parameter is $\mathbf{P} \cdot (\nabla \times \mathbf{M})$, electric polarization times bound current. Analyzing an effective field-theory displaying such order parameter without other symmetry breaking would shed further light on the properties of this class of isotropic magnetic materials.

Data availability

The data shown in the figures, as well as the code generating all of the data is available at [25].

Author contributions

D. V. proposed the initial project idea, all authors contributed to creating the research plan and later refining it. D. V. formulated the bulk invariants. A. A. and D. V. devised the microscopic system and the scalar time-reversal breaking mechanism. D. V. wrote the code generating amorphous structures and computing the spectral functions. A. A. wrote the code for constructing and solving the network models. H. S. performed the numerical simulations and wrote the manuscript with input from all authors. A. A. managed the project with input from all authors.

Acknowledgments

D. V. thanks Roderich Moessner for useful discussions. The authors thank Elizabeth Dresselhaus and Bjorn Sbierski for sharing their network model code. The authors thank Isidora Araya Day for helping to set up and perform Pymablock calculations. A. A. and H. S. were supported by NWO VIDI grant 016.Vidi.189.180 and by the Netherlands Organization for Scientific Research (NWO/OCW) as part of the Frontiers of Nanoscience program. D.V. was supported by the Swedish Research Council (VR), the Knut and Alice Wallenberg Foundation, and the Deutsche Forschungsgemeinschaft (DFG, German Research Foundation) under Germany's Excellence Strategy through the Würzburg-Dresden Cluster of Excellence on Complexity and Topology in Quantum Matter – ct.qmat (EXC 2147, project-id 57002544).

References

- [1] L. Šmejkal and T. Jungwirth, *Symmetry and Topology in Antiferromagnetic Spintronics*, pp. 267–298, Springer International Publishing, ISBN 978-3-319-97334-0, doi:10.1007/978-3-319-97334-0_9 (2018).
- [2] L. Šmejkal, J. Sinova and T. Jungwirth, *Emerging research landscape of altermagnetism*, Phys. Rev. X **12**, 040501 (2022), doi:10.1103/PhysRevX.12.040501.
- [3] L. Fu, *Topological crystalline insulators*, Phys. Rev. Lett. **106**, 106802 (2011), doi:10.1103/PhysRevLett.106.106802.
- [4] A. Lau and C. Ortix, *Novel topological insulators from crystalline symmetries.*, Eur. Phys. J. Spec. Top. **227**, 1309 (2018), doi:10.1140/epjst/e2018-800098-y.
- [5] K. Shiozaki and M. Sato, *Topology of crystalline insulators and superconductors*, Phys. Rev. B **90**, 165114 (2014), doi:10.1103/PhysRevB.90.165114.
- [6] D. Varjas, A. Lau, K. Pöyhönen, A. R. Akhmerov, D. I. Pikulin and I. C. Fulga, *Topological phases without crystalline counterparts*, Phys. Rev. Lett. **123**, 196401 (2019), doi:10.1103/PhysRevLett.123.196401.
- [7] Z. Ringel, Y. E. Kraus and A. Stern, *Strong side of weak topological insulators*, Phys. Rev. B **86**, 045102 (2012), doi:10.1103/PhysRevB.86.045102.
- [8] L. Fu and C. L. Kane, *Topology, delocalization via average symmetry and the symplectic anderson transition*, Phys. Rev. Lett. **109**, 246605 (2012), doi:10.1103/PhysRevLett.109.246605.
- [9] I. C. Fulga, B. van Heck, J. M. Edge and A. R. Akhmerov, *Statistical topological insulators*, Phys. Rev. B **89**, 155424 (2014), doi:10.1103/PhysRevB.89.155424.
- [10] H. Spring, A. Akhmerov and D. Varjas, *Amorphous topological phases protected by continuous rotation symmetry*, SciPost Physics **11**(2) (2021), doi:10.21468/scipostphys.11.2.022.
- [11] D. Varjas, T. Ö. Rosdahl and A. R. Akhmerov, *Qsymm: Algorithmic symmetry finding and symmetric Hamiltonian generation*, New J. Phys. **20**(9), 093026 (2018), doi:10.1088/1367-2630/aadf67.

- [12] I. Araya Day, S. Miles, D. Varjas and A. R. Akhmerov, *Pymablock*, doi:10.5281/zenodo.7995684 (2023).
- [13] Q. Marsal, D. Varjas and A. G. Grushin, *Topological weaire–thorpe models of amorphous matter*, Proceedings of the National Academy of Sciences **117**(48), 30260 (2020), doi:10.1073/pnas.2007384117.
- [14] A. Weiße, G. Wellein, A. Alvermann and H. Fehske, *The kernel polynomial method*, Rev. Mod. Phys. **78**, 275 (2006), doi:10.1103/RevModPhys.78.275.
- [15] D. Varjas, M. Fruchart, A. R. Akhmerov and P. M. Perez-Piskunow, *Computation of topological phase diagram of disordered $\text{pb}_{1-x}\text{sn}_x\text{Te}$ using the kernel polynomial method*, Phys. Rev. Res. **2**, 013229 (2020), doi:10.1103/PhysRevResearch.2.013229.
- [16] D. K. K. Lee and J. T. Chalker, *Unified model for two localization problems: Electron states in spin-degenerate landau levels and in a random magnetic field*, Physical Review Letters **72**(10), 1510 (1994), doi:10.1103/physrevlett.72.1510.
- [17] M. R. Zirnbauer, *Toward a theory of the integer quantum hall transition: Continuum limit of the chalker–coddington model*, Journal of Mathematical Physics **38**(4), 2007 (1997), doi:10.1063/1.531921.
- [18] J. T. Chalker and P. D. Coddington, *Percolation, quantum tunnelling and the integer hall effect*, Journal of Physics C: Solid State Physics **21**(14), 2665 (1988), doi:10.1088/0022-3719/21/14/008.
- [19] F. Evers and A. D. Mirlin, *Anderson transitions*, Reviews of Modern Physics **80**(4), 1355 (2008), doi:10.1103/revmodphys.80.1355.
- [20] R. E. Miles, *Random polygons determined by random lines on a plane*, Proc. Natl. Acad. Sci. U.S.A. **52**(4), 901 (1964), doi:10.1073/pnas.52.4.901.
- [21] F. de Juan, A. G. Grushin, T. Morimoto and J. E. Moore, *Quantized circular photogalvanic effect in Weyl semimetals*, Nature Communications **8**, 15995 (2017), doi:10.1038/ncomms15995, 1611.05887.
- [22] F. Flicker, F. de Juan, B. Bradlyn, T. Morimoto, M. G. Vergniory and A. G. Grushin, *Chiral optical response of multifold fermions*, Phys. Rev. B **98**, 155145 (2018), doi:10.1103/PhysRevB.98.155145.
- [23] A. Altland and M. R. Zirnbauer, *Nonstandard symmetry classes in mesoscopic normal-superconducting hybrid structures*, Phys. Rev. B **55**, 1142 (1997), doi:10.1103/PhysRevB.55.1142.
- [24] A. Agarwala and V. B. Shenoy, *Topological insulators in amorphous systems*, Phys. Rev. Lett. **118**, 236402 (2017), doi:10.1103/PhysRevLett.118.236402.
- [25] H. Spring, D. Varjas and A. R. Akhmerov, *Isotropic 3D topological phases with broken time-reversal symmetry*, doi:10.5281/zenodo.8212020, This work was supported by NWO VIDI grant 016.Vidi.189.180 (2023).
- [26] C. W. Groth, M. Wimmer, A. R. Akhmerov and X. Waintal, *Kwant: a software package for quantum transport*, New Journal of Physics **16**(6), 063065 (2014), doi:10.1088/1367-2630/16/6/063065.

- [27] H. C. Po, A. Vishwanath and H. Watanabe, *Symmetry-based indicators of band topology in the 230 space groups*, Nature Communications **8**(1) (2017), doi:10.1038/s41467-017-00133-2.
- [28] B. Bradlyn, L. Elcoro, J. Cano, M. G. Vergniory, Z. Wang, C. Felser, M. I. Aroyo and B. A. Bernevig, *Topological quantum chemistry*, Nature **547**(7663), 298 (2017), doi:10.1038/nature23268, 1703.02050.
- [29] T. Van Mechelen and Z. Jacob, *Quantum gyroelectric effect: Photon spin-1 quantization in continuum topological bosonic phases*, Phys. Rev. A **98**, 023842 (2018), doi:10.1103/PhysRevA.98.023842.

A Model Hamiltonians

We use Qsymm to generate 3D class A models that respect inversion symmetry and isotropic continuous rotation symmetry, whose symmetry representations are:

$$U_{\mathcal{I}} = \sigma_0 \tau_z, S_x = \frac{1}{2} \sigma_x \tau_0, S_y = \frac{1}{2} \sigma_y \tau_0, S_z = \frac{1}{2} \sigma_z \tau_0, \quad (\text{A.1})$$

where $U_{\mathcal{I}}$ is the unitary part of the inversion operator, $S_{x,y,z}$ are the generators of continuous spin rotations around the x , y , and z axes, and the unitary part of the corresponding rotation operator is given by $U = \exp(i\mathbf{n} \cdot \mathbf{S})$ with \mathbf{n} the axis and angle of rotation, and τ , σ are the Pauli matrices. τ represents the orbital component, and σ the spin component of the Hilbert space. The resulting model also has reflection symmetry on any 2D plane,

$$U_{\mathcal{M}_x} = i\sigma_x \tau_z, U_{\mathcal{M}_y} = i\sigma_y \tau_z, U_{\mathcal{M}_z} = i\sigma_z \tau_z, \quad (\text{A.2})$$

where $U_{\mathcal{M}_{x,y,z}}$ is the unitary part of the reflection operators on the planes perpendicular to the x , y and z axes, or in general,

$$U_{\mathcal{M}_{\hat{\mathbf{n}}}} = \exp(i\pi \hat{\mathbf{n}} \cdot \mathbf{S}) \tau_z, \quad (\text{A.3})$$

where $\hat{\mathbf{n}}$ is a unit vector defining the mirror normal. Because of the full rotation invariance, prescribing one mirror symmetry results in mirror symmetry with respect to any plane.

The generated k -space model is listed in the main text in Eq. (1). In real-space, the model is of the form:

$$H_{4 \times 4}^{\text{onsite}} = \mu_1 \sigma_0 (\tau_0 + \tau_z) / 2 + \mu_2 \sigma_0 (\tau_0 - \tau_z) / 2, \quad (\text{A.4})$$

$$H_{4 \times 4}^{\text{hopping}}(\mathbf{d}) = (tn_1 + t_2 d^2) \sigma_0 (\tau_0 + \tau_z) / 2 + (tn_2 + t_3 d^2) \sigma_0 (\tau_0 - \tau_z) / 2 \\ + (t_0 - t_5 d^2) \boldsymbol{\sigma} \cdot \mathbf{d} \tau_y + (t_1 + t_4 d^2) \boldsymbol{\sigma} \cdot \mathbf{d} \tau_x, \quad (\text{A.5})$$

where tn_i are normal hopping terms, $\mathbf{d} = (d_x, d_y, d_z)$, with d_i the bond lengths along axis $i \in \{x, y, z\}$ that connect neighboring sites, and $d^2 = \mathbf{d} \cdot \mathbf{d}$.

When demonstrating that symmetry-breaking gaps out the surface Dirac-nodes, we introduce a mass term that breaks all symmetries except for continuous rotation around the x axis:

$$\lambda = (\sigma_0 + \sigma_x) \tau_y. \quad (\text{A.6})$$

We also construct a doubled model. In k -space, this model takes the form:

$$\begin{aligned}
 H_{8 \times 8}(\mathbf{k}) = & 1/2(\rho_0 + \rho_z)\sigma_0(\mu_1(\tau_0 + \tau_z)/2 + \mu_2(\tau_0 - \tau_z)/2) \\
 & + 1/2(\rho_0 - \rho_z)\sigma_0(\mu_3(t\tau_0 + \tau_z)/2 + \mu_4(\tau_0 - \tau_z)/2) \\
 & + (t_0(\rho_0 + \rho_z)/2 + t_3(\rho_0 - \rho_z)/2)\boldsymbol{\sigma} \cdot \mathbf{k}\tau_x \\
 & - (t_4(\rho_0 + \rho_z)/2 + t_7(\rho_0 - \rho_z)/2)\boldsymbol{\sigma} \cdot \mathbf{k}\tau_y \\
 & + (t_1 + it_5)\rho_- \boldsymbol{\sigma} \cdot \mathbf{k}\tau_- + (t_1 - it_5)\rho_+(\boldsymbol{\sigma} \cdot \mathbf{k}\tau_-)^\dagger \\
 & + (t_2 + it_6)\rho_- \boldsymbol{\sigma} \cdot \mathbf{k}\tau_+ + (t_2 - it_6)\rho_+(\boldsymbol{\sigma} \cdot \mathbf{k}\tau_+)^\dagger,
 \end{aligned} \tag{A.7}$$

where μ_i are chemical potential terms, t_i are the hopping terms, ρ , σ and τ are the Pauli matrices, $\mathbf{k} = (k_x, k_y, k_z)$, and $k^2 = \mathbf{k} \cdot \mathbf{k}$. In real space, the model takes the form:

$$\begin{aligned}
 H_{8 \times 8}^{\text{onsite}} = & 1/2(\rho_0 + \rho_z)\sigma_0(\mu_1(\tau_0 + \tau_z)/2 + \mu_2(\tau_0 - \tau_z)/2), \\
 & + 1/2(\rho_0 - \rho_z)\sigma_0(\mu_3(\tau_0 + \tau_z)/2 + \mu_4(\tau_0 - \tau_z)/2) \\
 H_{8 \times 8}^{\text{hopping}}(\mathbf{d}) = & 1/2(\rho_0 + \rho_z)\sigma_0(tn_1(\tau_0 + \tau_z)/2 + tn_2(\tau_0 - \tau_z)/2) \\
 & + 1/2(\rho_0 - \rho_z)\sigma_0(tn_3(\tau_0 + \tau_z)/2 + tn_4(\tau_0 - \tau_z)/2) \\
 & + (it_0(\rho_0 + \rho_z)/2 + it_3(\rho_0 - \rho_z)/2)\boldsymbol{\sigma} \cdot \mathbf{d}\tau_x \\
 & - (it_4(\rho_0 + \rho_z)/2 + it_7(\rho_0 - \rho_z)/2)\boldsymbol{\sigma} \cdot \mathbf{d}\tau_y \\
 & + (-t_5 + it_2)\rho_- \boldsymbol{\sigma} \cdot \mathbf{d}\tau_- + (t_5 + it_2)\rho_+(\boldsymbol{\sigma} \cdot \mathbf{d}\tau_-)^\dagger \\
 & + (-t_6 + it_1)\rho_- \boldsymbol{\sigma} \cdot \mathbf{d}\tau_+ + (t_6 + it_1)\rho_+(\boldsymbol{\sigma} \cdot \mathbf{d}\tau_+)^\dagger,
 \end{aligned} \tag{A.8}$$

where tn_i are normal hopping terms, $\mathbf{d} = (d_x, d_y, d_z)$, with d_i the bond lengths along axis $i \in \{x, y, z\}$ that connect neighboring sites, and $d^2 = \mathbf{d} \cdot \mathbf{d}$. The symmetry-breaking term for the doubled model is

$$\lambda' = \begin{pmatrix} 1 & 1 \\ 1 & 1 \end{pmatrix} \otimes \begin{pmatrix} 1 & 1 \\ 1 & 1 \end{pmatrix} \otimes \tau_y. \tag{A.9}$$

B Model and plotting parameters

In this section additional details of the plots are listed in order of appearance.

For panel (c) of Fig. 1 the Hamiltonian (5) was simulated using kwant [26] on a translationally invariant 3D face-centered cubic (FCC) lattice. Its eigenvalues were obtained along the high-symmetry points of the FCC lattice, using the parameters $\mu_1 = 0.1$, $\mu_2 = 0.2$, $t_1 = 0.3$, $t_2 = -0.4$, $t_3 = \exp(0.3i)$, $t_4 = 0.2i \exp(0.3i)$. For the dispersion shown in panel (d), a slab was simulated, periodic along the vectors $[1, 0, 0]$ and $[0, 1, 0]$, and with a width of 20 sites in the $[0, 0, 1]$ direction. The parameters used are the same as for panel (c).

For panel (a) of Fig. 3, the Chalker-Coddington network is composed of four unit cells in both x and y . For panel (b), the amorphous network was created with an outer radius of $R = 20$, an inner radius of $r = 4$, and a density of 1. The positions of the nodes of the network underwent a relaxation step where the position of each node is sequentially averaged over the position of all neighboring nodes. For panel (d), the results for single-mode Chalker-Coddington network were obtained for 249 different random scattering matrix configurations, for network sizes of 36, 72, 144, 288, 576, 1152, 2304 and 4608 unit cells, with an aspect ratio of 1. The results for the two-mode Chalker-Coddington network were obtained for the same network sizes and aspect ratio, and for 269 different scattering matrix configurations. For the amorphous network, the results were obtained

for 50 outer radii sizes between $10^{1.5}$ and $10^{2.5}$, with a fixed outer radius over inner radius ratio of 1.5, and a density of 0.7. Results for the single mode network were obtained for 500 different amorphous network and scattering matrix configurations, and 300 different configurations for the two-mode amorphous network. Additional results for the single mode network were obtained for 5 outer radii sizes between $10^{2.5}$ and 10^3 , for 100 different network configurations and scattering matrices.

For Fig. 2(a), single-Dirac cone model as defined in Eq. (A.4) was used. Its parameters were set to $\mu_1 = -1$, $\mu_2 = 1$, $tn_1 = 0$, $tn_2 = 0$, $t_0 = 0.5$, $t_1 = 0.4$, $t_2 = 1$, $t_3 = -1$, $t_4 = 0.3$, $t_5 = 0.8$ and the additional symmetry-breaking term λ from Eq. (A.6) is set to 0. For panels (b) and (d) the same model as panel (a) was used. Its parameters were set to $\mu_1 = 1$, $\mu_2 = -1$, $tn_1 = -2$, $tn_2 = 2$, $t_0 = 1$, $t_1 = 1$, $t_2 = 1.1$, $t_3 = 1.2$, $t_4 = 1.3$, $t_5 = 1.25$ and the additional symmetry-breaking term λ from Eq. (A.6) is set to 0. The results were obtained for k -points between $-\pi$ and π . For panel (d) and (e), λ is set to 0.3. For the doubled model as defined in Eq. (A.8), the parameters were set to $\mu_1 = 1$, $\mu_2 = -1$, $\mu_3 = 1$, $\mu_4 = -1$, $tn_1 = -2$, $tn_2 = 2$, $tn_3 = -2$, $tn_4 = 2$, $\lambda_1 = 0.1$, $\lambda = 0.11$, $\lambda_3 = 0.12$, $\lambda_4 = 0.123$. The amorphous slab was generated in a box of dimensions $200 \times 50 \times 50$ and density 0.4.

For panel (a) of Fig. C.1, the model (A.4) was used. For all results, the hopping parameters were set to $t_0 = 1$, $t_1 = 1.2$, $t_2 = 0$, $t_3 = 0$, $t_4 = 0$, $t_5 = 0$, $tn_1 = -2$, $tn_2 = 2$ (terms proportional to k to the power of 2 and higher are set to 0). Since the only hopping terms are linear in d , in order to ensure that TRS is broken for this model, a different distance dependence is given for the t_1 and t_2 : $t_1 \exp(-0.3d)$ and $t_2 \exp(-d)$, where $d = \sqrt{d^2}$ is the bond length. The amorphous samples are all contained within a cube of $30 \times 30 \times 30$ sites, with a density of 0.7, and the crystal samples are all $10 \times 10 \times 10$ sites. For the invariant ν_M (6) the numerical integration over the Brillouin zone of the effective Hamiltonian was done over a grid of 15×15 points.

For panel (b) of Fig. C.1, the model (5) was used. The parameters were set to $t_1 = 0.3$, $t_2 = -0.4$, $t_3 = \exp(0.3i)$, $t_4 = i \exp(0.3i)$. The Γ and X points of the model are $(0, 0, 0)$ and $(0, 2\pi, 0)$.

C Alternative bulk invariants

In addition to the bulk invariant given in Sec. 3.1, we identify two alternative expressions.

C.1 Inversion eigenvalues

The inversion operator commutes with the spins at the rotation-invariant points $\mathbf{k} = \mathbf{0}$ and $\mathbf{k} = \infty$. Since the $SU(2)$ rotation symmetry commutes with the inversion operator, the inversion eigenvalues come in degenerate pairs in the case of a spin-1/2 representation, and in degenerate groups of $2s+1$ for spin- s representations. The difference in parity of the inversion eigenvalue pairs at these rotation-invariant points characterizes the topological phase:

$$\begin{aligned} \nu_I &= \frac{1}{2} [\nu_-(\infty) - \nu_-(\mathbf{0})], \\ \nu_-(\mathbf{k}) &= \mu_{-1} (\langle n(\mathbf{k}) | \mathcal{I} | m(\mathbf{k}) \rangle), \end{aligned} \tag{C.1}$$

where $|n(\mathbf{k})\rangle$ are the occupied states of the effective Hamiltonian H_{eff} , and $\mu_\lambda(A)$ indicates the multiplicity of the eigenvalue λ in the spectrum of A . We note that in the case of an operator that only has ± 1 eigenvalues, the multiplicity can be expressed through the

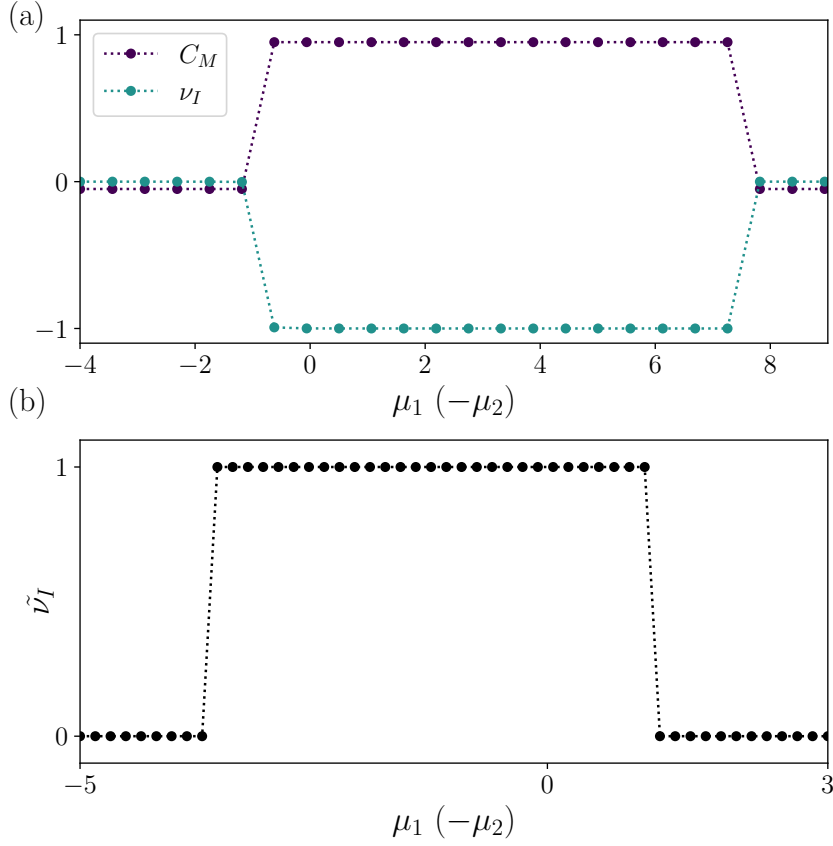


Figure C.1: Conductivity of translationally invariant and amorphous networks. (a) The topological invariants of the class A model (A.4) for amorphous systems (C_M defined in (6) and ν_I in (C.1)) as a function of chemical potentials $\mu_{1,2}$. Plots are offset for clarity. (b) The invariant $\tilde{\nu}_I$ of the crystal system as a function of chemical potentials $\mu_{1,2}$ (5). Plot details are in App. B.

trace as $\text{Tr } A = N - 2\mu_{-1}(A)$, allowing to rewrite the invariant as

$$\nu_I = -\frac{1}{4} \sum_{n \in \text{occ}} (\langle n(\infty) | \mathcal{I} | n(\infty) \rangle - \langle n(\mathbf{0}) | \mathcal{I} | n(\mathbf{0}) \rangle), \quad (\text{C.2})$$

where we used that the total number of occupied bands is the same at $\mathbf{k} = \mathbf{0}$ and ∞ .

While we only consider spin-1/2 representations in the main text, in the general case it is possible to resolve the eigenstates at $\mathbf{k} = \mathbf{0}$ and ∞ based on the spin-representation \mathbf{S} . All states along a line $\hat{n}\mathbf{k}$ connecting $\mathbf{0}$ and ∞ have continuous rotation symmetry along the \hat{n} axis, hence the eigenvalues of $\hat{n} \cdot \mathbf{S}$ in the occupied subspace are well-defined throughout, and the total number of various spin representations cannot change. The inversion eigenvalues, however, can change in the process, so we can define the set of invariants

$$\begin{aligned} \nu_I^s &= \frac{1}{2s+1} [\iota_-^s(\infty) - \iota_-^s(\mathbf{0})], \\ \iota_-^s(\mathbf{k}) &= \mu_{-1}(\langle n_s(\mathbf{k}) | \mathcal{I} | m_s(\mathbf{k}) \rangle), \end{aligned} \quad (\text{C.3})$$

where we restrict the inversion operator to the subspace corresponding to the spin- s representation spanned by the states $|n_s(\mathbf{k})\rangle$. This results in a \mathbb{Z}^N classification, of which the

invariant (C.1) only probes a \mathbb{Z} subset,

$$\nu_I = \sum_s \left(s + \frac{1}{2} \right) \nu_I^s. \quad (\text{C.4})$$

This relation also shows that, depending on the spin representation content of the model, not all values of ν_I may be realizable. A remaining question is, whether for general s , ν_I or the set of ν_I^s has a bulk-boundary correspondence in amorphous systems. As we show in the next section (see (C.9)), it is a different combination of ν_I^s that the mirror Chern invariant probes, nontrivial values of which we expect to protect robust surface states. The simplest continuum model with trivial ν_I (or C_M) and nontrivial ν_I^s has 16 on-site degrees of freedom (4 spin-1/2 and 2 spin-3/2 representations, half of which is inversion-odd), we leave analysis of the surface physics to future work.

For the crystalline system described in Sec. 2.3 we calculate the analogous eigenvalue parity invariant given by:

$$\tilde{\nu}_I = \frac{1}{2} [\iota_-(\Gamma) + \iota_-(X)] \pmod{4}, \quad (\text{C.5})$$

where ι is the same as in (C.1). The mod 4 results from factoring out atomic insulators located at other Wyckoff positions. We note that (C.5) does not give the full symmetry indicator classification in space group 225 [27, 28], and the \mathbb{Z} invariant given by the mirror Chern number also remains well defined and contains additional information.

C.2 Rotation eigenvalues

Another way to formulate the bulk invariant relies on the Chern-number being expressible through the difference in the occupied rotation eigenvalues at the rotation-invariant points $\mathbf{k} = \mathbf{0}$ and $\mathbf{k} = \infty$ [13, 29]:

$$C = \sum_{n \in \text{occ}} (\langle n(\infty) | S_z | n(\infty) \rangle - \langle n(\mathbf{0}) | S_z | n(\mathbf{0}) \rangle), \quad (\text{C.6})$$

where S_z is the generator of rotations around the z axis and the Chern-number is calculated in the $k_z = 0$ plane (other orientations give equivalent results). To formulate the mirror Chern number, we insert $-iM_z$, which adds a ± 1 prefactor to the mirror-even/odd states:

$$C_M = -\frac{1}{2} \sum_{n \in \text{occ}} (\langle n(\infty) | iM_z S_z | n(\infty) \rangle - \langle n(\mathbf{0}) | iM_z S_z | n(\mathbf{0}) \rangle). \quad (\text{C.7})$$

In general $M_z = \mathcal{I} \exp(i\pi S_z)$, in the spin-1/2 case this simplifies to $M_z = i\mathcal{I}\sigma_z$, hence $-iM_z S_z = \frac{1}{2}\mathcal{I}$. Substituting this, we find

$$C_M = \frac{1}{4} \sum_{n \in \text{occ}} (\langle n(\infty) | \mathcal{I} | n(\infty) \rangle - \langle n(\mathbf{0}) | \mathcal{I} | n(\mathbf{0}) \rangle) = -\nu_I. \quad (\text{C.8})$$

For general spin, using that \mathcal{I} commutes with the spin operators, after some algebra we find

$$\begin{aligned} C_M &= \frac{1}{4} \sum_s (-1)^{s-\frac{1}{2}} \sum_{n_s \in \text{occ}_s} (\langle n_s(\infty) | \mathcal{I} | n_s(\infty) \rangle - \langle n_s(\mathbf{0}) | \mathcal{I} | n_s(\mathbf{0}) \rangle) \\ &= \sum_s (-1)^{s+\frac{1}{2}} \left(s + \frac{1}{2} \right) \nu_I^s. \end{aligned} \quad (\text{C.9})$$

As we saw, in the spin-1/2 case studied in detail, Eqs. (6, (C.7), and (C.1)) are all equivalent formulations of the same invariant, as demonstrated by their equivalence for different values of the chemical potential [Fig. C.1(a)].

D Amorphous network model

In order to ensure four-fold coordination of each node of the amorphous network, we generate the network following the method described in Refs. [13, 20], which creates a graph by generating N random lines on a plane, with N chosen from a Poisson distribution whose mean is set to $2R\sqrt{\pi\rho}$, with ρ the chosen density of the graph and R the outer radius of the network. The angle and offset of the lines is uniformly distributed in $[0, 2\pi)$ and $[0, R]$ respectively. We define the intersections of each pair of lines as a network node. We ensure the two-in-two-out pattern of propagating modes at each node by orienting the links in an alternating fashion along each of the straight lines. There is no dependence of the scattering matrices on the length of the network links.

The graph is cut into an annulus shape by removing all of the nodes beyond the outer radius R and within the inner radius r . This ensures periodic boundary conditions along the polar angle coordinate. In order to maintain four-fold connectivity in the bulk of the graph, the nodes outside of the network that are connected to nodes inside of the network are changed into sinks or sources, that either absorb modes from the network or emit modes to the network. The conductivity of the amorphous network is calculated by $g = G \ln(R/r)/2\pi$, with $G = (e^2/h) \sum_{i,j} |S_{ij}|^2$, S_{ij} being the matrix element of the scattering matrix that connects the incoming modes originating from external sources beyond the network's outer edge to the outgoing modes exiting the network from its inner edge. A relaxation of the graph for visual clarity is optionally performed by averaging each node position to the center of its neighbors' positions.